



Microstructural and nanoindentation study of spark plasma sintered high entropy alloy reinforced aluminium matrix composites

Smith Salifu^{*}, Peter Apata Olubambi

Centre for Nanoengineering and Advanced Materials, University of Johannesburg, South Africa

ARTICLE INFO

Keywords:

High entropy alloy
CALPHAD
Spark plasma sintering
Nanoindentation
Al matrix composites

ABSTRACT

In this study, Spark Plasma Sintering (SPS) also known as a field-assisted technique was employed in the fabrication of high entropy alloy (HEA) reinforced aluminium matrix composites (using 5, 7 and 10 wt% HEA as the reinforcement in the composites); and conventional methods were employed to determine the relative density and microhardness; while nanoindentation technique was employed to determine the nanohardness, modulus of elasticity and nanoindentation depth of the sintered samples. Calculation Phase Diagram (CALPHAD) software, Thermocalc was employed in the prediction of the phases present in the HEA, while XRD was used in the confirmation of the phases. The phase analysis showed that BCC, FCC, and laves are the phases present in the fabricated HEA while the microstructural analysis showed that interdiffusion layers were formed; and atomic precipitation that resulted in the formation of new phases occurred during sintering. The microhardness, nanohardness, and modulus of elasticity of the sintered HEA-reinforced Al matrix composites increase with an increase in the wt% of HEA such that as little as 5 wt% HEA addition resulted in a 102.8 % increment in microhardness, while the densification and indentation depth were discovered to decrease with an increase in the wt% of HEA.”

1. Introduction

The field of materials science and engineering has witnessed remarkable advancements in recent years. This has resulted in the development of innovative materials with properties tailored towards the use in diverse applications. Among these novel materials, high entropy alloys (HEAs) [1] and metal matrix composites (MMCs) have emerged as captivating areas of research and exploration due to their unique properties. Unlike conventional alloys, HEAs are characterized by a unique composition with multiple principal elements (usually greater than or equal to 5) [1,2]. The unconventional composition of HEAs results in them exhibiting exceptional mechanical, thermal, and corrosion-resistant properties [2,3]. Thus, making them promising candidates for various engineering applications. On the other hand, MMCs have enjoyed enormous patronage in the research world in recent times due to their improved properties derived from the combination of metals or metals and other heterogeneous materials [4]. MMCs are composite materials consisting of a metallic matrix reinforced with a secondary phase, and the synergy between the metal matrix and the reinforcement phases imparts desirable attributes such as improved

strength, stiffness, wear resistance, and thermal performance [4]. This concept of reinforcement has been applied successfully in various industrial sectors, including aerospace, automotive, and structural engineering, where lightweight, high-strength materials are in demand [5, 6].

The incorporation of HEAs into metal matrix composites (MMCs) is expected to present an intriguing avenue that would further enhance the material properties and expand the scope of application of the developed MMCs [7]. Furthermore, the outstanding properties of HEAs such as good ductility and high modulus of elasticity have popularized their use as a special reinforcement for aluminium matrix [8,9]. In a study conducted by Chen et al. [10], AlCoNiCrFe was successfully used to reinforce pure aluminium matrix via mechanical alloying, and the tensile strength of the aluminium matrix composites (AMCs) was higher than that of the aluminium matrix.

AlCoCrFeNi HEA was used by Li et al. [11], to reinforce AA5083 aluminium plates via a fusion stir processing technique. The fabricated composite exhibited a significant enhancement in its mechanical properties as compared to the AA5083 aluminium matrix [11]. Furthermore, the fabrication process was also discovered to have a significant effect on

* Corresponding author.

E-mail address: smithsalifu@gmail.com (S. Salifu).

the mechanical and microstructural properties of the developed AMCs [12–14]. Tan et al. [15], employed the spark plasma sintering (SPS) technique in the consolidation of Al0.6CoCrFeNi particles reinforced Al-based amorphous composites, and a high compressive yield strength was obtained in the composite when compared to the Al-matrix. In a similar study conducted by Liu et al. [16], the SPS technique was employed in the fabrication of aluminium matrix-reinforced AlCoCrFeNi HEA particles. The outcome of the study showed that an increase in the sintering temperature of the composites resulted in an increase in the interfacial layer and a significant improvement in the plasticity and yield strength of the composites was also observed.

Vacuum hot pressing technique was employed by Chen et al. [17], in the preparation of AlCoNiCrFe HEA particles reinforced copper matrix, and no obvious interfacial reaction was observed between the matrix and the HEA particles. Nevertheless, the yield strength of the composites of the HEA-reinforced copper matrix is close to that predicted by the Vioigt model. Wang, Yan, et al. [7], used the rotation friction extrusion (RFE) in the fabrication of CrMnFeCoNi HEA reinforced Al-matrix composites. During the fabrication process using the RFE technique, the HEA particles reacted with the Al matrix and numerous FCC phases were formed due to the high thermodynamic driving force that aids the interdiffusion of the elements that make up the HEA. Compared to the Al-matrix, the tensile strength of the AMCs was substantially enhanced.

In the realm of materials science, nanoindentation has emerged as a fast and pivotal nondestructive method for assessing mechanical properties [18,19]. Several studies have been conducted on HEA and HEA-reinforced metal matrix composites with a focus on their bulk properties [20,21]. Since the surface of materials acts as the initial or first point of contact during service [22], it is paramount to evaluate the surface properties of the fabricated HEA-reinforced Al-matrix composites in order to provide accurate and necessary information that will complement the existing pool of bulk properties of HEA and HEA-reinforced metal matrix composites in the open literature. In the assessment of the surface properties of materials, the nanoindentation technique has proved to be effective [23–25]. In previous studies conducted by Olorundaisi et al. [26], Zhang et al. [27], and Dada et al. [28] it was discovered that the nanoindentation technique can provide adequate information on the load-bearing and the anti-wear behavior of SPSed HEA, HEA-reinforced 316 L stainless steel composite, and HEA coating, respectively.

In this study, the promising material paradigms of aluminium (matrix) and high entropy alloys (reinforcement) were leveraged to develop high entropy alloy reinforced Al-matrix composites consolidated using the spark plasma sintering technique, and the microstructural, mechanical, and nanomechanical properties of the metal matrix composites were determined.

2. Methodology

2.1. Processing of HEA and HEA-reinforced Al matrix composites

In the fabrication of the CuNiMnCrCoNb HEA-reinforced Al-matrix composites, spherical aluminium powder with about 99.8% purity was used as the matrix while metallic powder of Cu, Ni, Mn, Cr, Co, and Nb, with purity greater than 99% and with particle size $\leq 25\mu\text{m}$ was used to develop the HEA used as the reinforcement. The powder particles of the elements that make the HEA were milled in a planetary milling (Retsch Planetary ball mill PM 400 220–230 V, 50/60 Hz) machine for 4 hours at a milling speed of 200 RPM, and paused for 10 min at an interval of 30 min. Thereafter, the appropriate wt% of the milled HEA was mixed with Al-matrix in a tubular mixer for 24 hours at a frequency of 50 Hz. Depicted in Table 1 is the atomic percentage of the composition of the elements that make up the HEA and Table 2 shows the composition of the composites sintered.

During the milling of the HEA and the mixing of the HEA-reinforced Al matrix composites, a 250 ml stainless steel jar and stainless steel balls

Table 1
HEA powder composition.

Elements	Cu	Ni	Mn	Cr	Co	Nb
Atomic %	20	20	20	20	10	10

Table 2
wt% of HEA and pure Al used in the development of the HEA-reinforced Al matrix composites.

S/N	wt% HEA	wt% pure Al
1	5.0	95.0
2	7.0	93.0
3	10.0	90.0

with 8 mm diameter were employed such that a 10:1 ball-to-powder ratio was used to improve the homogeneity of the mixed powder. The well-mixed HEA-reinforced as shown in Table 2 are consolidated using the field-assisted SPS technique, by employing the HHPD 5, FCT Germany field-assisted sintering machine. A high-strength and highly heat-resistant 20 mm diameter graphite die was employed during the sintering of the composites. The samples were sintered at a temperature of 500 °C, a holding time of 10 min, sintering rate of 100°C/min and a sintering pressure of 50 MPa. Thereafter, the mixed HEA-reinforced Al matrix composite powders and consolidated samples were subjected to different characterization. The sintering parameters for the HEA-reinforced Al matrix composites were carefully chosen and conducted under an inert atmosphere to ensure optimal densification while minimizing the potential for interfacial reactions between the HEA and the Al matrix.

Using 100gf load at a duration of 15 s, the INNOVATEST FALCON 500 microhardness tester was used to determine the Vickers microhardness of the consolidated samples. The indentation of the samples was done 10 times at random positions on each sample and the average Vickers hardness of each of the consolidated samples was obtained. An electronic densometer that uses Archimedes' principle was employed in the determination of the densification of the consolidated samples.

An X-ray diffractometer (PW1710 Philips, PANalytical Empyrean model) with $\lambda = 0.15406 \text{ nm}$ (Cu Ka radiation), 30.0 mA accelerating current and 40.0 kV voltage was employed for the analysis of the well-mixed powder and consolidated samples. During the analysis, a scanning speed of 1.50 deg/min and a scanning range between 5° and 90° were used for the phase analysis of the consolidated samples and well-mixed powders. In the microstructural characterization of the mixed powders and consolidated samples, an FE-SEM: JEOL JSM 7600 F energy-dispersive equipped Scanning Electron Microscope (SEM) was employed.

2.2. Spark plasma sintering

The sintering profile for the HEA-reinforced Al matrix composites as recorded by the SPS machine is depicted in Fig. 1. Based on the recorded data for the sintering profile, a distinct relationship was observed between the sintering time, punch displacement, and sintering temperature. Since the initial temperature of the SPS furnace is 250 °C (as read by the attached sensitive pyrometer connected within the furnace), the sintering of the HEA-reinforced Al matrix composites starts at 250 °C while the displacement of the punch and sintering temperature at 0 min as shown in Fig. 1. From the figure, five distinct stages were identified with the first stage characterised by spark creation between the powder particles and the removal of gas, which occurs within the first 2 min of sintering without any noticeable punch movement [29]. The second stage lasted for approximately 4 min (spanning from 1 to 5 min), and the stage was characterised by a rise in sintering temperature from 250 °C to about 255 °C with a significant linear displacement of the punch. Stage

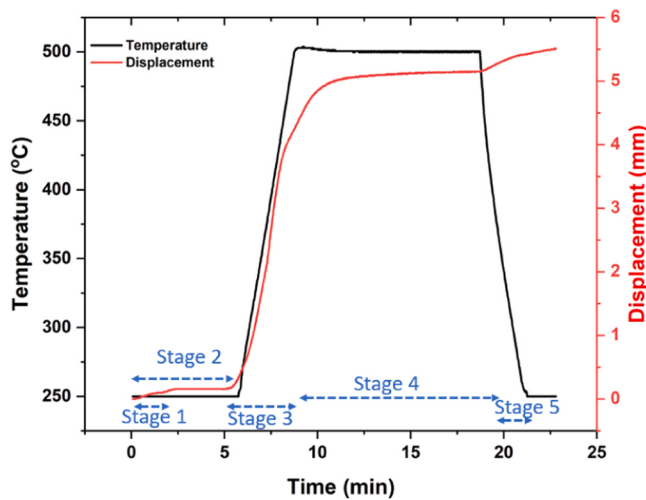


Fig. 1. SPS sintering profile of HEA-reinforced Al matrix composite.

three (3) lasted for about 3 min starting from the 5th to the 8th minute. This stage was characterised by the compaction of the powder particles, necking, and bulk or complete powder particle deformation. Stage 4 lasted for approximately 10 min, and it is characterised by a swift punch movement the sintering temperature rises from 255 – 475 °C, after which the punch displacement remains constant and no further particle deformation was observed despite the applied pressure. However, through the phenomenon of mass transport, neck growth occurs in this stage and the powder particles sintering finally occur [30,31] as the voids (between adjacent necks) are closed due to the punch movement caused by the applied pressure. The last stage involves the cooling down of the sintered sample which lasted for 3 min.

2.3. Nanoindentation analysis

Adopting the ASTM E3–11 standard, the sintered samples were subjected to metallographic operation prior to the conduction of nano-indentation analysis to determine their indentation depth, nanohardness and elastic modulus, using the Anton-Parr “Hit 300” nanoindenter system which uses the Berkovich diamond indenter for the indentation. Fused silica (with an already established modulus of elasticity and Poisson’s ratio) was used in the calibration of the pointed tip of the indenter, while the Berkovich indenter was selected as the indentation tip because of the ease of gridding the tip to the required sharp point [32]. Also, Oliver and Pharr [33] technique was adopted using a load of 200 mN, a loading and unloading time of 1 200 mN and a holding time of 10 s was used to perform the analysis. With the equipment operated under force-controlled configuration as stated in ISO 14577 [34], both the indentation load and the indentation depth as a function of time were recorded, and the average modulus of elasticity and nanohardness of the samples were determined from 10 indentations conducted on each of the samples.

According to Olive and Pharr, the expression for the determination of nanohardness (H) and reduced modulus of elasticity (E_r) is given as follows [35]:

$$H = \frac{P_{\max}}{A_c} \quad (1)$$

where P_{\max} represents the maximum applied load, and A_c represents the indentation area given by

$$A_c = P(h_c^2) \quad (2)$$

where P represents the applied load, and h_c represents the depth at the maximum load

Expression for the relationship between the maximum load, P_{\max} , maximum depth, h_{\max} and contact depth, h_c is given as follows:

$$h_c = h_{\max} - \varepsilon \frac{P_{\max}}{S} \quad (3)$$

where the value of ε is 1.5 for the Berkovich indenter, and S represents the contact stiffness which can be obtained from the curve of the unloading slope using the following expression:

$$S = \left(\frac{dp}{dh} \right) = \beta \frac{2}{\sqrt{\pi}} E_r \sqrt{A_c} \quad (4)$$

where $\frac{dp}{dh}$ represents the slope in the curve elastic region during unloading, and β represents the diamond-shaped triangular geometric factor of the Berkovich indenter, whose value is 1.034 [18].

Thus, the expression for the reduced elastic modulus, E_r is given as follows:

$$\frac{1}{E_r} = \frac{1 - \nu^2}{E} + \frac{1 - \nu_i^2}{E_i} \quad (5)$$

where E_i and ν_i represents the modulus of elasticity and Poisson’s ratio of the Berkovich indenter, respectively, and the modulus of elasticity and Poissons ratio of the samples are E and ν , respectively.

3. Results and discussions

3.1. Phase prediction and microstructure

In the design of HEAs, the accurate prediction of the possible stable phase/phases formed helps in the determination of the possible areas of applications. To determine/predict the stable phases formed in HEAs, Yang [36] and Guo et al. [37,38], devise mechanisms that favour the formation of stable BCC, FCC or the combination of both phases. According to the authors, the expressions for the determination of the stable phase/phase during HEA development, and the predicted values and phases obtained for the HEA developed in this study are shown in Table 3.

Calculation Phase Diagram (CALPHAD) software, Thermocalc was employed to predict the phases present in the HEA used as reinforcement in the composites. During the phase prediction, the TCHEA2 database was used and the predicted phases are shown in Fig. 2. Since the sintering temperature of the HEA-reinforced Al matrix composite is less than 600 °C, the predicted phases in the HEA within the sintering temperature are required. From Fig. 2, BCC, FCC, and laves were the possible phases predicted by the Thermocalc software, and these phases are the possible phases expected to be present in the sintered HEA-reinforced Al matrix composites. The Valence Electron Concentration (VEC) value of 8.20 obtained in Table 3 for the HEA suggested that FCC phase is present and stable. This was corroborated by the CALPHAD prediction which indicated FCC as the more stable phase. In addition to the very stable FCC phase, the CALPHAD prediction indicated the presence of a slightly stable BCC phase at higher moles and a temperature of 500 °C. The prediction of the slightly stable BCC phase by the CALPHAD software and corroborated by the XRD results suggest that the energy difference between the two phases is relatively small within the temperature and range of composition used. While the FCC phase is more stable, the difference in the Gibbs energy between the two phases is not sufficient enough to completely suppress the formation of the BCC phase. In a related study, CALPHAD software was used in the confirmation of the VEC calculation and the phases present in HEA [45,46].

3.2. Microstructure and phase analysis of HEA-reinforced Al matrix composites

The pure Al, milled HEA and HEA-reinforced Al matrix composites

Table 3

Expression for determination of stable phase/phases and the predicted values and phases for the HEA developed in this study.

S/ N	Equations	Parameters	Comments	Values obtained
1	$\Omega = \frac{T_m \Delta S_{mix}}{\Delta H_{mix}}$	T_m is melting temperature, ΔS_{mix} is mixing entropy and ΔH_{mix} is mixing enthalpy.	The value of Ω must be greater than or equal to 1.10 ($\Omega \geq 1.10$) for solid solution HEA to be formed.	6.90
2	$\delta = \sqrt{\sum_{i=1}^n (c_i(1 - r_i/\bar{r}))^2}$	c_i is ith element atomic ratio, r_i is ith element radius and \bar{r} is the average atomic radius, n is the number of elements that make up the HEA.	The value of δ must be $\leq 6.6\%$ ($\delta \leq 6.6\%$), in order to promote the formation of solid solution HEA [37].	5.53%
3	$\Delta H_{mix}^{ij} = \sum_{i=1, i \neq j}^n 4 \Delta H_{ij}^{mix} c_i c_j$	ΔH_{ij}^{mix} is the ith and jth element mixing enthalpy.	If the condition $-15 < \Delta H_{mix} < 5 \text{ kJ/mol}$, HEA is considered stable [39,40].	3.16 kJ/mol
4	$T_{mix} = \sum_{i=1}^n c_i (T_m)_i$	$(T_m)_i$ is the ith element melting point.	T_{mix} is the predicted melting point of the HEA.	1535 °C
5	$\Delta S_{mix} = -R \sum_{i=1}^n (c_i \ln c_i)$	R is the gas constant, 8.314 J/K.mol.	If the condition $12 \leq \Delta S \leq 17.5 \text{ J/K}$, HEA is considered stable [39,40].	14.21 J/K
6	$VEC = \sum_{i=1}^n c_i (VEC)_i$	VEC is the Valence Electron Concentration, c_i is ith element atomic ratio and n is the number of elements that make up the HEA.	If $VEC \geq 8$, FCC phase is stable, if $VEC \leq 6.87$, BCC phase is stable, and if $6.87 < VEC < 8$, both FCC and BCC phases are stable [41–44].	8.20

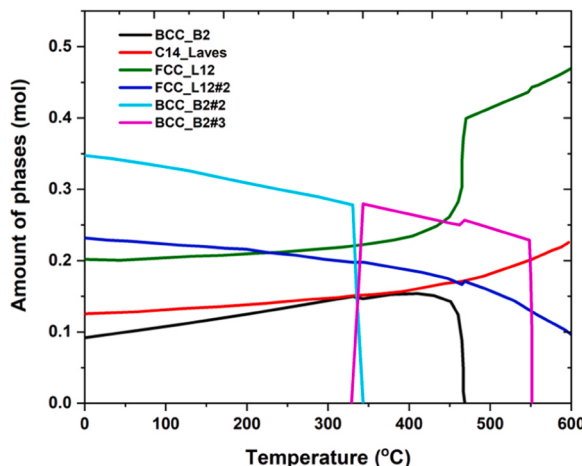


Fig. 2. CALPHAD predicted phases for HEA.

powder SEM micrograph and XRD results are shown in Fig. 3. From the micrograph of the pure Al (depicted in Fig. 3(a)), the powder is found to consist of well-dispersed smooth surfaced spherical particles similar to those reported by Chen et al. [47]. Fig. 3(b) shows the micrograph of the HEA powder which has a mixed blend of spherical, potato-like and flat-shaped particles that are relatively mixed uniformly. In a related study conducted by Yim et al. [48], similar irregular shapes and morphology were obtained and the shapes and morphology have high flowability [49,50] and thus, are capable of affecting the physical and mechanical properties of the high entropy alloy and the composites formed when they are used as reinforcement [51]. The micrograph of the composite powder with respect to the wt% of the HEA is shown in Fig. 3(c-e). On all the large particle sizes of the composite powder developed, spherical satellites were observed on their surface, and the larger the size of the particles, the rougher the surface is [52]. Fig. 3(f) shows the XRD pattern of the pure Al, HEA and the composite powders formed. In addition to the FCC and BCC phases that were identified in the milled powder of the HEA and the HEA-reinforced Al matrix, peaks of Cr₂Nb intermetallic phase were also identified and all the elements that HEA and the Aluminium matrix were present either in the BCC structure, FCC structure or Cr₂Nb intermetallics formed upon milling. In a related study conducted by Yuan et al. [53] and Liu et al. [54], on CoCrFeNiMo_{0.2} and CoCrCuFeNi, reinforced Ti matrix composites, respectively, after ball-milling for 0.5–6 hours, XRD powder pattern similar to the one reported in this study were obtained.

Fig. 4(a)-(d) shows the SEM micrograph of the sintered pure Al and HEA-reinforced Al matrix composites. The grey surface represents the aluminium-rich region, the white and light grey surfaces represent the

BCC and FCC HEA phases, respectively, while the dark spots randomly distributed across the micrographs represent the laves phase. In the SEM micrographs, the different contrast indicates how electrons are absorbed or scattered. While the white region on the micrograph indicates areas where the electrons are strongly absorbed, the dark or grey regions of the image indicate areas where electrons are less absorbed or scattered. The HEA particles (both coarse and fine) are fairly distributed homogeneously within the aluminium matrix such that the level of homogeneity improves with an increase in the HEA content in the matrix. Pockets of porosity were observed in the sintered samples without any other form of imperfections such as flaws and/or cracks. The absence of these other defects signifies an improvement in the sintering technique for the fabrication of the samples [55]. Depicted in Fig. 4(e) is the XRD of the sintered sample which shows the presence of the Al-matrix phase, BCC phase, FCC phase, and laves in all the composites sintered by the presence of their characteristic peaks. The broad peaks of the BCC HEA, FCC HEA and the lave phases indicate that their phases are disordered. Compared to the XRD pattern of the pure sintered Al, a slight shift was detected in the peak of the composites, and this shift is a result of the stress and strain induced when HEA was added to the Al matrix. The stress induced by the addition of the HEA slightly alters the interplanar spacing and the XRD pattern. During sintering, precipitation of the atoms of the HEA occurs and these atoms react with the Al-matrix to form new phases (laves) [53], as shown in the XRD result in Fig. 4(e). These new phases formed during sintering imply that a level of interfacial occurs between the Al-matrix and the HEA.

During milling/mixing, the HEA particles were not subjected to severe deformation, however, there was diffusion between the Al-matrix and HEA particles as depicted by the diffusion layer between the HEA and Al-matrix in the EDS line scan in Fig. 4(f). Two different colors are exhibited by the diffusion layer (the color of the inner layer is light grey while the color of the outer layer (closer to HEA) is dark grey). The quantity of the elements and their intensity along the scanned region are determined by the magnitude and the fluctuation of the k factor, respectively. Between 0 and 13 μm, and 22–40 μm on the line scan, the distribution of the elements is not equal. This suggests that the individual elements may diffuse to each other near the interface during sintering, and this may lead to possible segregation if the missing entropy between the combining elements is not sufficient to balance their mixing enthalpy. However, between 13 and 22 μm, the distribution of the elements that make up the HEA-reinforced Al matrix composites is approximately the same. This implies that the mixing entropy and enthalpy of the element at the region is almost the same and segregation may not occur at the region.

3.3. Microhardness and relative density

Fig. 5 depicts a plot of the microhardness and relative density of the

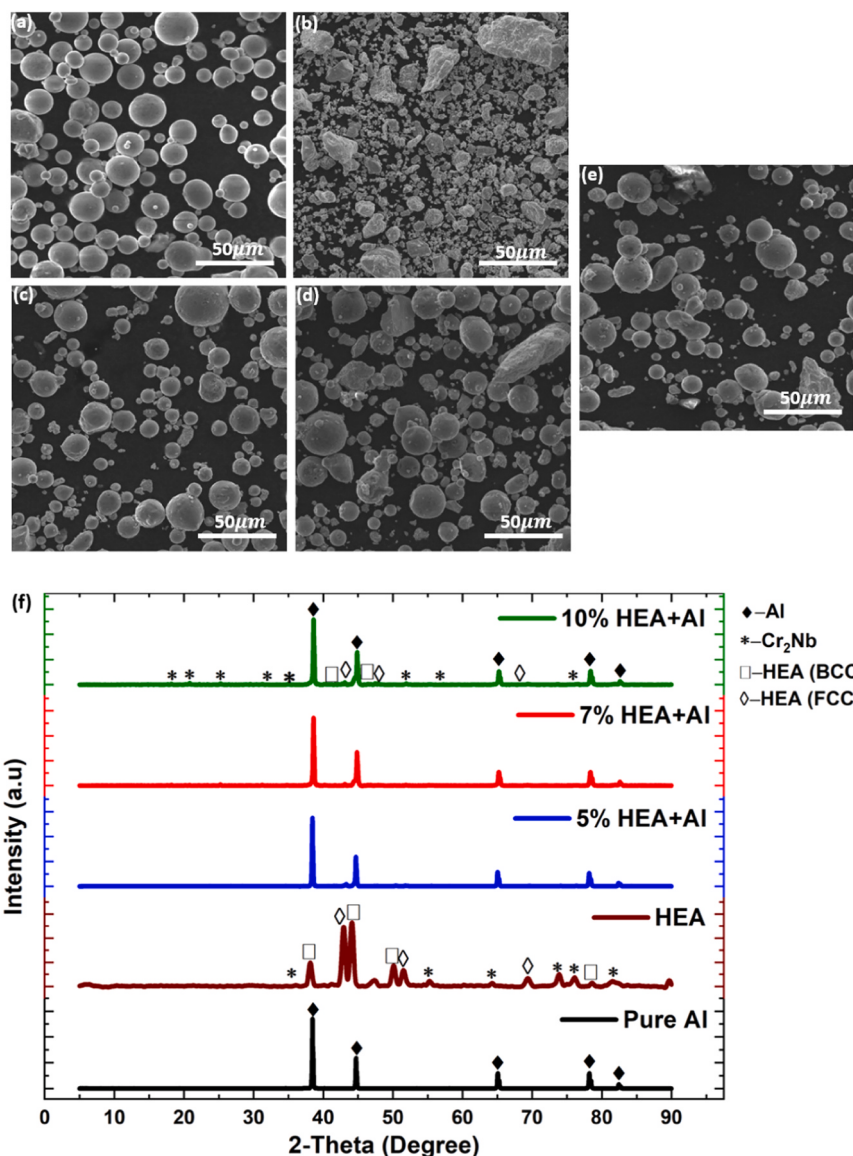


Fig. 3. SEM micrograph of (a) Pure Al-Powder (b) HEA-Powder (c) 5% HEA + Al-Powder (d) 7% HEA + Al-Powder and (e) 10% HEA + Al-Powder at 500 magnification; and (f) XRD of the powders.

sintered composite matrix with respect to the wt% of the reinforcement (HEA). From the plots, it was discovered that as the wt% of the reinforcement was increased, the value of the microhardness of the composites also increased such that the pure Al without any reinforcement had the least microhardness with a value of 35.8 HV, while the composite with 5 wt% reinforcement has a microhardness value of 72.3 HV (about 102.8% higher than the microhardness of pure Al). When the wt % of the reinforcement was increased to 7 and 10%, respectively, the microhardness of the developed composites was 82.4 and 96.0 HV, respectively and this value is about 130% and 168%, respectively higher than that of pure Al. The improvement in the microhardness of the composites with an increase in the wt% of the reinforcement (HEA) can be attributed to the unique properties introduced by the HEA as well as the interdiffusion layer formed which assisted in sintering defects reduction [53].

On the other hand, the relative density of the composites decreases with an increase in the wt% of the reinforcement such that the pure Al has the highest relative density (98.6%) while the composite with 10 wt % reinforcement has the least relative density (98.1%). Although the sintering technique adopted for the consolidation of the composites is

expected to improve their densification, the densification of the sintered samples was improved but the improvement in the densification was observed to decrease with an increase in the reinforcement. The decrease in the densification of the sintered composite with an increase in the wt% of the reinforcement could be likened to the increase in atomic inhomogeneity with an increase in the HEA reinforcement in the composites, and the increase in the inhomogeneity greatly affects the atomic packing, aid pores formation and reduce the sintered samples [45].

3.4. Nanoindentation load-displacement and depth-time plots for sintered pure Al and HEA-reinforced Al matrix composites

Depicted in Fig. 6 is the nanoindentation load-depth plot for the sintered pure Al and HEA reinforced Al matrix composites with 200 mN load, 1 200 mN/mins loading and unloading rate, and 10 s holding time. The shape of the plots obtained for the pure Al and the composites is an indication that the indented pure Al and HEA-reinforced Al matrix composites behaved in an elastic-plastic manner upon the application of the indentation force by the nanoindenter. As shown in Fig. 6, a direct

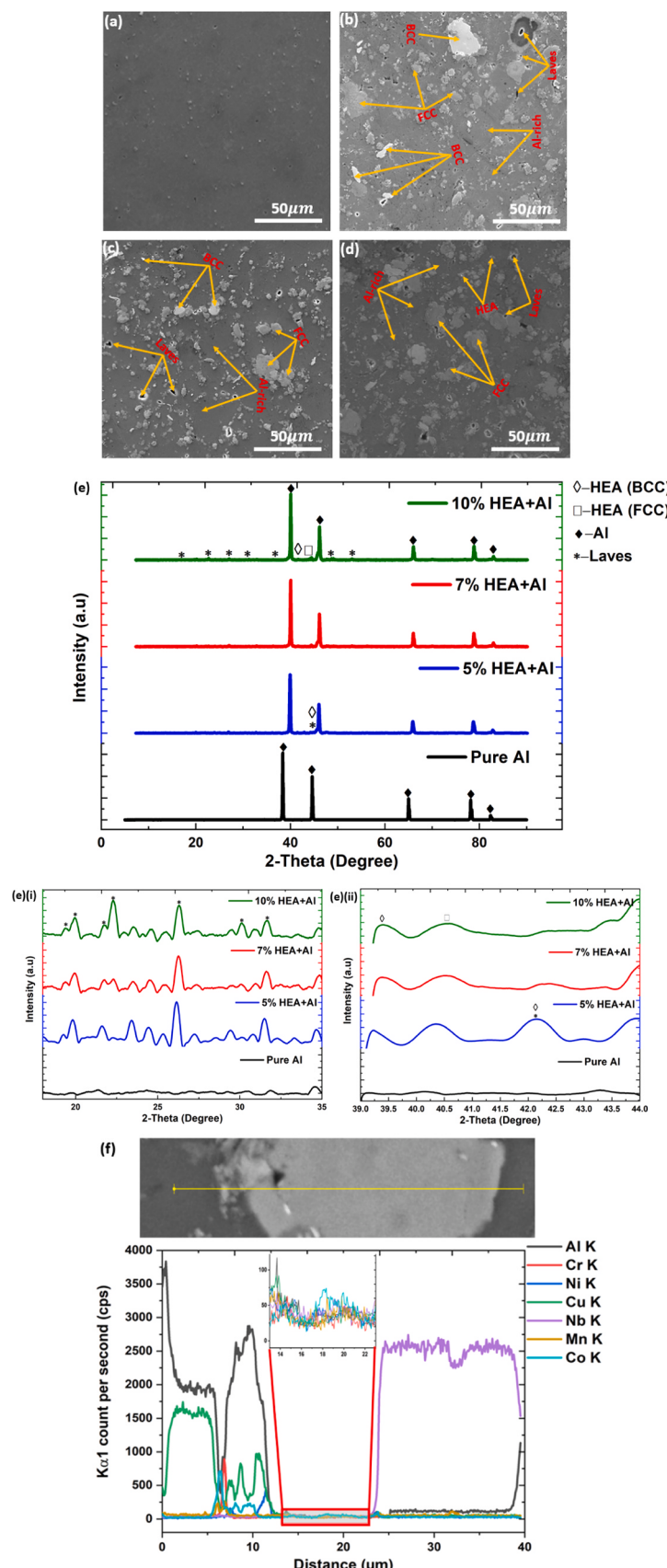


Fig. 4. SEM micrograph of sintered (a) Pure Al, (b) 5% HEA + Al, (c) 7% HEA + Al, (d) 10% HEA + Al at 500 magnification, (e) XRD of the sintered samples; and (f) line scan EDS in the region with interdiffusion layer and the corresponding plot for the composite matrix with 7% HEA.

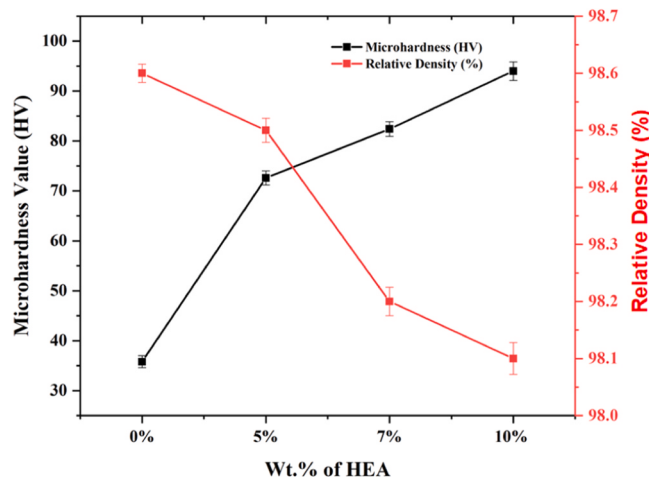


Fig. 5. Microhardness and density of HEA-reinforced Al-matrix composites as a function wt% of HEA addition.

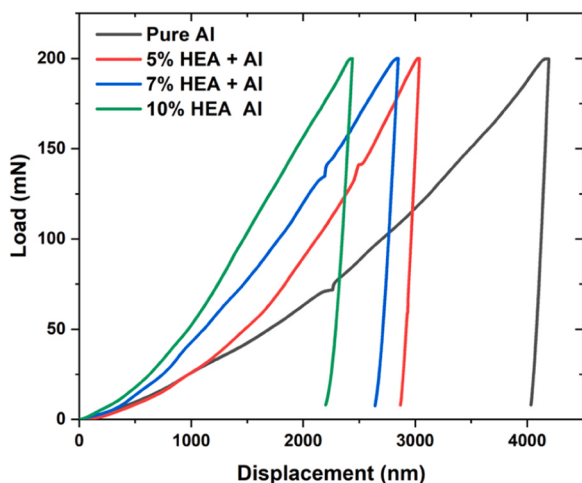


Fig. 6. Nanoindentation load-depth plot of pure Al and HEA-reinforced Al matrix composites at 200 mN applied load.

relationship exists between the applied indentation load and the indentation depth such that the indentation depth increases with an increase in the applied indentation load. Also, a significant indentation depth reduction was observed with an increase in the wt% of HEA in the composites such that pure Al has the highest indentation depth while the composite with 10 wt% HEA has the least indentation depth under the applied indentation load. This implies that the addition of HEA as reinforcement to pure Al significantly increases the resistance of the composites formed to plastic deformation [56]. Hence, the stiffness and hardness of the composites are expected to be enhanced as compared to that of the pure Al due to the effective transfer of load from the matrix to the reinforcement.

Fig. 7 shows a plot of the nanoindentation depth time for the sintered pure Al and HEA-reinforced Al matrix composites when subjected to 200 mN indentation load. From the plot, it was observed that the indentation depth at every point in time increases with a decrease in the wt% of the HEA in the composite such that the pure Al has the highest indentation depth (4100 nm) while the composite with 10 wt% HEA has the least indentation depth (2300 nm). This behavior displayed by the composites can be ascribed to the increased dislocation resistance which occurs due to the increase in the hard HEA phases in the composite's matrix [56]. Thus, the higher the wt% of HEA phases in the composites, the lower the depth of penetration, and the slightly higher the

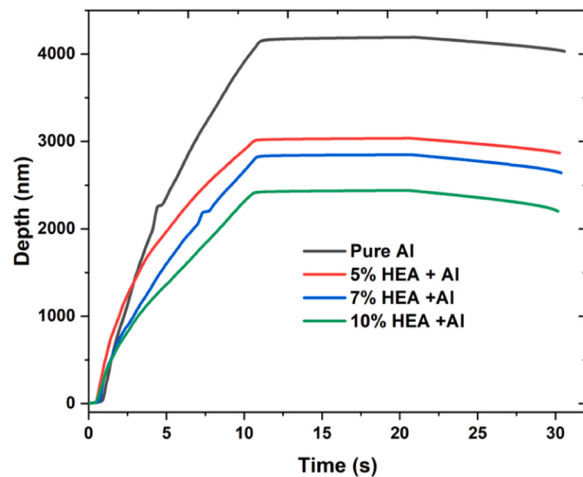


Fig. 7. Depth-time indentation plot for pure Al and HEA-reinforced Al matrix composite at 200 mN applied load.

indentation/penetration time required.

3.5. Nanoindentation hardness and elastic modulus of the SPSed pure Al and HEA-reinforced Al matrix composites

Depicted in Fig. 8 are the nanohardness and elastic modulus of the SPSed pure Al and HEA-reinforced Al matrix under an indentation load of 200 mN. From the figure, the nanohardness and modulus of elasticity were noticed to increase with an increase in the wt% of HEA, such that the composite with 10 wt% HEA has the highest microhardness (2949.2 MPa) and modulus of elasticity (128.99 GPa), while the pure Al has the least nanohardness (470.53 MPa) and modulus of elasticity (66.66 GPa). The nanohardness results obtained for the developed composites follow the same trend as those of the microhardness in Fig. 5. According to Wheeler [57], the increase in the modulus of elasticity of material with an increase in reinforcement results in an increase in the stiffness of such material with an increase in reinforcement since the stiffness of a material is proportional to its modulus of elasticity. The significant improvement in the elastic modulus and nanohardness of the HEA-reinforced Al composite matrix as compared to the pure, unreinforced Al can be attributed to the fact that the tip of the indenter during nanoindentation generates a sudden and large amount of activities, and it is also the main source of dislocation, which usually results in accumulation of strain [58]. In addition to this, the presence of hard HEA

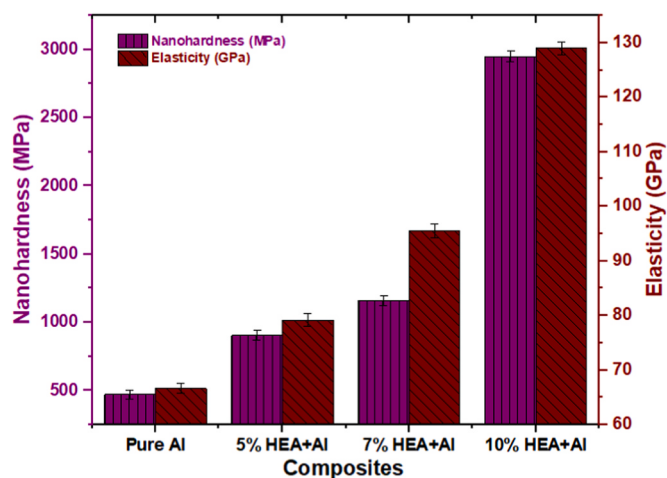


Fig. 8. Nanohardness and modulus of elasticity of pure Al and HEA-reinforced Al matrix composites.

phases and the intermetallic phases formed within the composites hinder the movement of dislocation. This is because, during the sintering of HEA-reinforced Al matrix composites, the presence of hard HEA phases and intermetallic phases can primarily result in the generation of screw dislocations, and these dislocations contribute to strain hardening of the composites as they pile-up at the grain boundaries when their movements are hindered.

4. Conclusion

In this study, spark plasma sintering (field-assisted) technique was employed in the fabrication of pure Al and HEA-reinforced Al matrix composites. The relative density and microhardness of the sintered samples were determined using a densometer and microhardness tester while the nanomechanical properties of the developed samples were investigated by employing the nanoindentation technique. The CALPHAD predicted the presence of BCC phase, FCC phase and laves; and was confirmed by the peaks of the XRD results obtained during the phase analysis of the HEA and HEA-reinforced Al matrix composites. The microstructure of the sintered samples showed that atomic precipitation occurs and new phases were formed due to the reaction of the atoms from the HEA with the surrounding Al matrix. Furthermore, interdiffusion layer, Al dominated and HEA-rich regions were observed on the sintered composites. Although the SPS technique used in this study improved the densification of the sintered composites, the relative density of the composites slightly decreased with an increase in the wt% of the HEA such that the pure Al has the highest densification with a value of 98.6 while the composite with 10 wt% HEA has the least densification with a value of 98.1%. Poor atomic packing emanating from the higher inhomogeneity introduced when the wt% of the HEA increases in the composite is thought to be responsible for this behavior. At room temperature, the addition of HEA to the pure Al matrix increases the microhardness of the composites formed such that just 5 wt % HEA addition to the pure Al resulted in about 102.8% increment in microhardness value when compared to that of the pure Al, while 7 and 10 wt% addition of HEA to pure Al resulted in about 130 and 168% increment, respectively. Just like the microhardness, the nanohardness of the composites increases with an increase in the wt% of HEA. Similarly, the elastic modulus of the composites increases with an increase in the wt% of HEA such that the pure Al has the least modulus of elasticity while the composite with 10 wt% has the highest modulus of elasticity. The nanoindentation depth of the composites decreases with an increase in the wt% of the HEA, thus indicating that the higher the wt% of HEA in the composite, the higher the resistance to any form of indentation.

Ethics approval

Not applicable.

Consent to participate

Not applicable.

Consent for publication

All authors have read and agreed to publish the manuscript.

CRediT authorship contribution statement

Smith Salifu: Conceptualization, Investigation, Methodology, Writing – original draft. **Peter Apata Olubambi:** Software, Supervision, Writing – review & editing.

Declaration of Competing Interest

The authors declare that they have no known competing financial

interests or personal relationships that could have appeared to influence the work reported in this paper.

Data Availability

Data will be made available on request.

Acknowledgments

The authors acknowledge Global Excellence and Stature (GES 4.0) and the Centre for Nanoengineering and Advanced Materials, University of Johannesburg, South Africa, for their immense support.

References

- [1] H. Wang, J. Xie, Y. Chen, W. Liu, W. Zhong, Effect of CoCrFeNiMn high entropy alloy interlayer on microstructure and mechanical properties of laser-welded NiTi/304 SS joint, *J. Mater. Res. Technol.* vol. 18 (2022) 1028–1037.
- [2] D.B. Miracle, O.N. Senkov, A critical review of high entropy alloys and related concepts, *Acta Mater.* vol. 122 (2017) 448–511.
- [3] Q. Guo, H. Hou, K. Wang, M. Li, P.K. Liaw, Y. Zhao, Coalescence of Al0.3CoCrFeNi polycrystalline high-entropy alloy in hot-pressed sintering: a molecular dynamics and phase-field study, *npj Computational Materials* 9 (1) (2023) 185. <https://doi.org/10.1038/s41524-023-01139-9>.
- [4] P.V. Reddy, G.S. Kumar, D.M. Krishnudu, H.R. Rao, Mechanical and wear performances of aluminium-based metal matrix composites: a review, *J. Bio. Trib. Corros.* vol. 6 (3) (2020) 83.
- [5] V. Mohanavel, P. Periyasamy, M. Balamurugan, T. Sathish, A review on mechanical and tribological behaviour of aluminium based metal matrix composites, *Int. J. Mech. Prod. Eng. Res. Develop.* (2018) 473–478.
- [6] Song, J., Chen, Y., Hao, X., Wang, M., Ma, Y.,..., Xie, J. (2024). Microstructure and mechanical properties of novel Ni–Cr–Co-based superalloy GTAW joints. *Journal of Materials Research and Technology*, 29, 2758-2767. doi: <https://doi.org/10.1016/j.jmrt.2024.01.241>.
- [7] Y. Wang, et al., High entropy alloy reinforced aluminum matrix composites prepared by novel rotation friction extrusion process: microstructure and mechanical properties, *Mater. Sci. Eng. A* vol. 854 (2022) 143789.
- [8] Y.F. Zhao, Y.Q. Wang, K. Wu, J.Y. Zhang, G. Liu, J. Sun, Unique mechanical properties of Cu/(NbMoTaW) nanolaminates, *Scr. Mater.* vol. 154 (2018) 154–158.
- [9] G.M. Karthik, S. Panikar, G.D.J. Ram, R.S. Kottada, Additive manufacturing of an aluminum matrix composite reinforced with nanocrystalline high-entropy alloy particles, *Mater. Sci. Eng.: A* vol. 679 (2017) 193–203.
- [10] W. Chen, et al., Effect of ball milling on microstructure and mechanical properties of 6061Al matrix composites reinforced with high-entropy alloy particles, *Mater. Sci. Eng. A* vol. 762 (2019) 138116.
- [11] J. Li, et al., Friction stir processing of high-entropy alloy reinforced aluminum matrix composites for mechanical properties enhancement, *Mater. Sci. Eng. A* vol. 792 (2020) 139755.
- [12] M. Balakrishnan, I. Dinaharan, R. Palanivel, R. Sathiskumar, Influence of friction stir processing on microstructure and tensile behavior of AA6061/Al3Zr cast aluminum matrix composites, *J. Manuf. Process.* vol. 38 (2019) 148–157.
- [13] M. Balakrishnan, I. Dinaharan, K. Kalaiselvan, R. Palanivel, Friction stir processing of Al3Ni intermetallic particulate reinforced cast aluminum matrix composites: microstructure and tensile properties, *J. Mater. Res. Technol.* vol. 9 (3) (2020) 4356–4367.
- [14] S.A. Sajjadi, H.R. Ezatpour, H. Beygi, Microstructure and mechanical properties of Al-Al2O3 micro and nano composites fabricated by stir casting, *Mater. Sci. Eng. A* vol. 528 (29-30) (2011) 8765–8771.
- [15] Z. Tan, L. Wang, Y. Xue, P. Zhang, T. Cao, X. Cheng, High-entropy alloy particle reinforced Al-based amorphous alloy composite with ultrahigh strength prepared by spark plasma sintering, *Mater. Des.* vol. 109 (2016) 219–226.
- [16] Y. Liu, J. Chen, Z. Li, X. Wang, X. Fan, J. Liu, Formation of transition layer and its effect on mechanical properties of AlCoCrFeNi high-entropy alloy/Al composites, *J. Alloy. Compd.* vol. 780 (2019) 558–564.
- [17] J. Chen, et al., Fabrication and mechanical properties of AlCoNiCrFe high-entropy alloy particle reinforced Cu matrix composites, *J. Alloy. Compd.* vol. 649 (2015) 630–634.
- [18] H. Attar, et al., Nanoindentation and wear properties of Ti and Ti-TiB composite materials produced by selective laser melting, *Mater. Sci. Eng.: A* vol. 688 (2017) 20–26.
- [19] S. Ehtemam-Haghghi, G. Cao, L.-C. Zhang, Nanoindentation study of mechanical properties of Ti based alloys with Fe and Ta additions, *J. Alloy. Compd.* vol. 692 (2017) 892–897.
- [20] S. Salifu, P.A. Olubambi, Effects of fabrication techniques on the mechanical properties of high entropy alloys: a review, *Int. J. Lightweight Mater. Manuf.* (2023).
- [21] Guo, Q., Hou, H., Pan, Y., Pei, X., Song, Z., Liaw, P. K.,..., Zhao, Y. (2023). Hardening-softening of Al0.3CoCrFeNi high-entropy alloy under nanoindentation. *Materials & Design*, 231, 112050. doi: <https://doi.org/10.1016/j.matdes.2023.112050>.
- [22] Z. Zhang, J. Chen, J. Wang, Y. Han, Z. Yu, Q. Wang, S. Yang, Effects of solder thickness on interface behavior and nanoindentation characteristics in Cu/Sn/Cu

- microbumps. Welding in the, World 66 (5) (2022) 973–983, <https://doi.org/10.1007/s40194-022-01261-0>.
- [23] A. Leyland, A. Matthews, On the significance of the H/E ratio in wear control: a nanocomposite coating approach to optimised tribological behaviour, Wear vol. 246 (1-2) (2000) 1–11.
- [24] J. Xu, G. dong Wang, X. Lu, L. Liu, P. Munroe, Z.-H. Xie, Mechanical and corrosion-resistant properties of Ti–Nb–Si–N nanocomposite films prepared by a double glow discharge plasma technique, Ceram. Int. vol. 40 (6) (2014) 8621–8630.
- [25] J. Musil, F. Kunc, H. Zeman, H. Polakova, Relationships between hardness, Young's modulus and elastic recovery in hard nanocomposite coatings, Surf. Coat. Technol. vol. 154 (2-3) (2002) 304–313.
- [26] E. Olorundai, et al., Phase prediction, microstructure, and mechanical properties of spark plasma sintered Ni–Al–Ti–Mn–Co–Fe–Cr high entropy alloys, Discov. Nano vol. 18 (1) (2023) 117.
- [27] X. Zhang, D. Yang, Y. Jia, and G. Wang, Microstructure and Nanoindentation Behavior of FeCoNiAlTi High-Entropy Alloy-Reinforced 316L Stainless Steel Composite Fabricated by Selective Laser Melting, Materials, vol. 16, no. 5. ([doi:10.3390/ma16052022](https://doi.org/10.3390/ma16052022)).
- [28] M. Dada, P. Popoola, N. Mathe, S. Adeosun, S. Pityana, Investigating the elastic modulus and hardness properties of a high entropy alloy coating using nanoindentation, Int. J. Lightweight Mater. Manuf. vol. 4 (3) (2021) 339–345.
- [29] E. Ghasali, K. Shirvanimoghaddam, A.H. Pakseresht, M. Alizadeh, T. Ebadzadeh, Evaluation of microstructure and mechanical properties of Al-TaC composites prepared by spark plasma sintering process, J. Alloy. Compd. vol. 705 (2017) 283–289.
- [30] M. Tokita, The potential of spark plasma sintering (SPS) method for the fabrication on an industrial scale of functionally graded materials, Adv. Sci. Technol. vol. 63 (2011) 322–331.
- [31] A.L. Rominiyi, M.B. Shongwe, E.N. Ogunmuyiwa, B.J. Babalola, P.F. Lepele, P. A. Olubambi, Effect of nickel addition on densification, microstructure and wear behaviour of spark plasma sintered CP-titanium, Mater. Chem. Phys. vol. 240 (2020) 122130.
- [32] G.M. Pharr, Measurement of mechanical properties by ultra-low load indentation, Mater. Sci. Eng.: A vol. 253 (1-2) (1998) 151–159.
- [33] W.C. Oliver, G.M. Pharr, An improved technique for determining hardness and elastic modulus using load and displacement sensing indentation experiments, J. Mater. Res. vol. 7 (6) (1992) 1564–1583.
- [34] X. Li, B. Bhushan, A review of nanoindentation continuous stiffness measurement technique and its applications, Mater. Charact. vol. 48 (1) (2002) 11–36.
- [35] A.L. Rominiyi, P.M. Mashinini, Nanoindentation study of mechanical and wear properties of spark plasma sintered Ti-6Ni-xTiCN composites, Ceram. Int. vol. 49 (2) (2023) 2194–2203.
- [36] X. Yang, Y. Zhang, Prediction of high-entropy stabilized solid-solution in multi-component alloys, Mater. Chem. Phys. vol. 132 (2) (2012) 233–238.
- [37] S. Guo, C. Ng, J. Lu, C.T. Liu, Effect of valence electron concentration on stability of fcc or bcc phase in high entropy alloys, J. Appl. Phys. vol. 109 (10) (2011) 103505.
- [38] R.M. Pohan, et al., Microstructures and mechanical properties of mechanically alloyed and spark plasma sintered Al0.3CoCrFeMnNi high entropy alloy, Mater. Chem. Phys. vol. 210 (2018) 62–70, 2018/05/01/.
- [39] X. Yang, Y. Zhang, Prediction of high-entropy stabilized solid-solution in multi-component alloys, Mater. Chem. Phys. vol. 132 (2-3) (2012) 233–238.
- [40] M. Wu, et al., Investigation of mechanical properties and wear resistance of A2/B2 type medium-entropy alloy matrix reinforced with tungsten particles by in-situ reaction, Metals vol. 13 (4) (2023) 656.
- [41] A. Kumar, M. Gupta, An insight into evolution of light weight high entropy alloys: a review, Metals vol. 6 (9) (2016) 199.
- [42] A. Takeuchi, A. Inoue, Calculations of mixing enthalpy and mismatch entropy for ternary amorphous alloys, Mater. Trans., JIM vol. 41 (11) (2000) 1372–1378.
- [43] S. Yadav, K. Biswas, A. Kumar, Spark Plasma Sintering of High Entropy Alloys, in: P. Cavalieri (Ed.), in Spark Plasma Sintering of Materials: Advances in Processing and Applications, Springer International Publishing, Cham, 2019, pp. 539–571.
- [44] S. Salifu, P.A. Olubambi, L. Teffo, Phase stability and microstructural properties of high entropy alloy reinforced aluminium matrix composites consolidated via spark plasma sintering, Heliyon vol. 10 (2) (2024).
- [45] S.R. Oke, O.E. Falodun, A. Bayode, U.S. Anamu, P.A. Olubambi, Phase prediction, densification, and microstructure of AlCrFeNi(TiO₂)_x high entropy alloy composite fabricated by spark plasma sintering, J. Alloy. Compd. vol. 968 (2023) 172030.
- [46] U.S. Anamu, et al., Fundamental design strategies for advancing the development of high entropy alloys for thermo-mechanical application: a critical review, J. Mater. Res. Technol. vol. 27 (2023) 4833–4860.
- [47] H. Chen, Q. Yao, Q. Liu, H. Liu, X. Zhang, Effects of moisture content on the minimum explosive concentration of aluminum powder and the related mechanism, J. Energy vol. 2020 (2020) 1–10.
- [48] D. Yim, et al., Compaction behavior of water-atomized CoCrFeMnNi high-entropy alloy powders, Mater. Chem. Phys. vol. 210 (2018) 95–102.
- [49] Z. Ren, et al., Preparation and microstructure of multi-component high entropy alloy powders fabricated by gas atomization method, Metals vol. 13 (2) (2023) 432.
- [50] S. Wang, Y. Li, D. Zhang, Y. Yang, S.M. Manladan, Z. Luo, Microstructure and mechanical properties of high strength AlCoCrFeNi2. 1 eutectic high entropy alloy prepared by selective laser melting (SLM), Mater. Lett. vol. 310 (2022) 131511.
- [51] Y.A. Alshataif, S. Sivasankaran, F.A. Al-Mufadi, A.S. Alaboodi, H.R. Ammar, Manufacturing methods, microstructural and mechanical properties evolutions of high-entropy alloys: a review, Met. Mater. Int. vol. 26 (8) (2020) 1099–1133.
- [52] A. Fu, B. Liu, B. Liu, Y. Cao, J. Wang, T. Liao, Y. Liu, A novel cobalt-free oxide dispersion strengthened medium-entropy alloy with outstanding mechanical properties and irradiation resistance, Journal of Materials Science & Technology 152 (2023) 190–200. <https://doi.org/10.1016/j.jmst.2022.11.061>.
- [53] Z. Yuan, H. Liu, Z. Ma, X. Ma, K. Wang, X. Zhang, Microstructure and properties of high entropy alloy reinforced titanium matrix composites, Mater. Charact. vol. 187 (2022) 111856.
- [54] L. Liu, et al., Microstructure and mechanical properties of CoCrCuFeNi high-entropy alloys synthesized by powder metallurgy and spark plasma sintering, J. Mater. Eng. Perform. (2023).
- [55] E.A. Ananiadis, A.E. Karantzalis, A.K. Sifakis, E. Georgatis, T.E. Matikas, Aluminium matrix composites reinforced with AlCrFeMnNi HEA particulates: microstructure, mechanical and corrosion properties, Materials vol. 16 (15) (2023) 5491.
- [56] Y. Shadangi, K. Chattopadhyay, N.K. Mukhopadhyay, Powder metallurgical processing of Al matrix composite reinforced with AlSiCrMnFeNiCu high-entropy alloys: microstructure, thermal stability, and microhardness, J. Mater. Res. vol. 38 (1) (2023) 248–264.
- [57] J.M. WheelerNanoindentation under dynamic conditions, 2009.
- [58] L. Dekhil, S. Louidi, M. Bououdina, M. Fellah, Microstructural, magnetic, and nanoindentation studies of the ball-milled Ti80Ni20 alloy, J. Supercond. Nov. Magn. vol. 32 (2019) 3623–3636.